AGU PUBLICATIONS

JGR

Journal of Geophysical Research: Solid Earth

RESEARCH ARTICLE
10.1002/2017JB015195

Special Section:
Magnetism in the Geosciences - Advances and Perspectives

Magnetic Domain State Diagnosis in Soils, Loess, and Marine Sediments From Multiple First-Order Reversal Curve-Type Diagrams

P. X. Hu[1], X. Zhao[1], A. P. Roberts[1], D. Heslop[1], and R. A. Viscarra Rossel[2]

[1]Research School of Earth Sciences, Australian National University, Canberra, ACT, Australia, [2]CSIRO Land and Water, Canberra, ACT, Australia

Key Points:
- We provide the first extensive assessment of remanent, transient, and induced FORC diagrams for soil and marine sediments
- These additional diagrams are diagnostically powerful and assist magnetic domain state diagnosis
- By using transient FORC diagrams, we demonstrate that particles occur routinely in the magnetic vortex state

Correspondence to:
P. X. Hu,
pxhu1987@gmail.com

Citation:
Hu, P. X., Zhao, X., Roberts, A. P., Heslop, D., & Viscarra Rossel, R. A. (2018). Magnetic domain state diagnosis in soils, loess, and marine sediments from multiple first-order reversal curve-type diagrams. *Journal of Geophysical Research: Solid Earth*, *123*, 998–1017. https://doi.org/10.1002/2017JB015195

Received 6 NOV 2017
Accepted 24 JAN 2018
Accepted article online 27 JAN 2018
Published online 12 FEB 2018

Abstract First-order reversal curve (FORC) diagrams provide information about domain states and magnetostatic interactions that underpin paleomagnetic interpretations. FORC diagrams are a complex representation of remanent, induced, and transient magnetizations that can be assessed individually using additional FORC-type measurements along with conventional measurements. We provide the first extensive assessment of the information provided by remanent, transient, and induced FORC diagrams for a diverse range of soil, loess/paleosol, and marine sediment samples. These new diagrams provide substantial information in addition to that provided by conventional FORC diagrams that aids comprehensive domain state diagnosis for mixed magnetic particle assemblages. In particular, we demonstrate from transient FORC diagrams that particles occur routinely in the magnetic vortex state. Likewise, remanent FORC diagrams provide information about the remanence-bearing magnetic particles that are of greatest interest in paleomagnetic studies.

1. Introduction

First-order reversal curve (FORC) diagrams (Pike et al., 1999; Roberts et al., 2014, 2000) are used widely for diagnosing magnetic domain states, magnetostatic interaction field distributions, and interaction types in a wide range of magnetic materials analyzed in geophysics, solid-state physics, and materials science. Their principal benefit is that they enable identification of each of these types of features for individual magnetic components within measured samples, which removes many of the ambiguities associated with bulk magnetic measurements of samples that contain complex magnetic mineral mixtures. With application of magnetic unmixing techniques, interpretation of the rich information provided by FORC diagrams is becoming increasingly quantitative and powerful (e.g., Channell et al., 2016; Egli et al., 2010; Harrison & Lascu, 2014; Heslop et al., 2014; Lascu et al., 2015; Plaza-Morlote et al., 2017). Nevertheless, FORC diagrams are determined from in-field measurements that provide a complex representation of remanent, induced, and transient magnetizations. Zhao et al. (2017) described a range of FORC-type measurements in addition to conventional measurements that enable separation of each of these components. The resulting remanent FORC, transient FORC, and induced FORC diagrams provide substantial additional information that is valuable for understanding magnetic particle assemblages. For example, the remanence-bearing component is of greatest interest in paleomagnetic studies and is most clearly evident in the remanent FORC diagram of Zhao et al. (2017). When particles are too large to be in the stable single-domain (SD) magnetic state, they transition into a vortex state and then into the multidomain (MD) state. Transient FORC diagrams provide much clearer diagnostic information about the presence of vortex state and MD particles than conventional FORC diagrams (Zhao et al., 2017), and their wider use should prove to be powerful for understanding the real extent of the vortex state in natural materials (Roberts et al., 2017).

Much of the information that can be obtained from the additional FORC-type measurements described by Zhao et al. (2017) remains to be exploited, and in some cases the information remains to be fully understood. Considerable additional work is needed to unlock the full power of these additional measurement types. Here we present the first systematic analysis of wide-ranging soil, loess, and marine sediment samples to document the range of their magnetic properties and to demonstrate the interpretive power of the information provided by such measurements. Our results are valuable for diagnosing the full range of domain states in natural samples, particularly the prevalence of the magnetic vortex state.

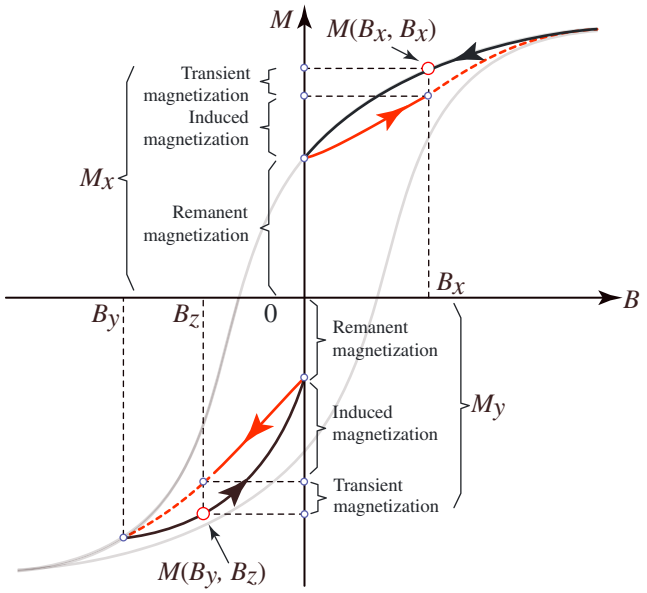

Figure 1. Definitions of the different types of magnetization discussed in this paper from a schematic hysteresis loop (modified from Zhao et al., 2017). The black lines with arrows indicate paths of changing magnetizations during hysteresis measurements (e.g., a major hysteresis loop or a FORC). The red lines with arrows indicate magnetization paths that start or pass through zero field, which give the transient-free magnetization. Transient magnetizations must be present in magnetization paths that decrease to zero field (black line) or in reversal curves for which the reversal field is not zero or of opposite sign.

2. Measurements, Interpretational Framework, and Materials

The information provided by FORC-type measurements (Zhao et al., 2017) is not yet widely understood. Thus, we provide details of the measurement protocols and interpretive framework below for the additional FORC-type diagrams and the samples analyzed for this study.

2.1. FORC, Remanent FORC, and Transient-Free FORC Measurements

FORC diagrams are calculated from a class of partial magnetic hysteresis curves known as FORCs (Mayergoyz, 1991). A sample is first saturated magnetically in a strong positive field (B_{sat}). The field is then decreased to a reversal field (B_r), and a FORC is measured at a series of applied fields, B, from B_r to B_{sat}. Multiple FORCs are measured for a series of B_r values to obtain the gridded magnetization measurements used to create a FORC diagram (Roberts et al., 2000, 2014). Magnetization data from consecutive measurement points on consecutive FORCs are used to determine the FORC distribution, which is defined as a mixed second derivative (Mayergoyz, 1991; Pike et al., 1999; Roberts et al., 2014). Calculation of a second derivative amplifies measurement noise, so that smoothing is generally necessary to obtain a meaningful FORC distribution. The smoothing factor (SF) represents the grid of $(2SF + 1)^2$ data points over which smoothing is performed. The FORC distribution is then represented by smoothed data and is plotted using a continuously varying color map. FORC diagrams are presented in terms of the interaction field B_i and coercivity B_c distributions using the transformations $B_i = (B_r + B)/2$ and $B_c = (B - B_r)/2$. To first approximation, a FORC diagram is a plot of the magnetic switching field (coercivity) and local interaction field distributions of measured particles. This information is used to diagnose the magnetic domain states of magnetic minerals (Egli et al., 2010; Pike et al., 1999, 2001; Roberts et al., 2000, 2006, 2014).

We used the irregularly spaced field step measurement protocol of Zhao et al., (2015) to produce high-resolution FORC diagrams. With the irregular grid protocol, data are measured at more closely spaced field steps over regions with larger magnetization gradients and vice versa. Therefore, larger numbers of measurements are made in key regions of a FORC distribution to resolve diagnostic features at the required resolution. The form of a FORC distribution is not known a priori, so the measurement grid is defined from a slope-corrected major hysteresis loop (Zhao et al., 2015). Following Zhao et al. (2017), we use the irregular grid measurement protocol and present the resulting conventional FORC, remanent FORC (remFORC), induced FORC (iFORC), and transient FORC (tFORC) diagrams to enable identification of magnetic signatures associated with each domain state in soil, loess, and marine sediment samples.

Instead of using in-field magnetization measurements, a remFORC diagram is obtained using remanent magnetization measurements by sweeping the magnetic field to a specified value and back to zero after each applied field step (Figure 1). The concept of transient hysteresis was introduced by Fabian (2003) and represents the difference between the ascending and descending branches of partial hysteresis loops when cycled from saturation to the remanent state, and then back to saturation (Figure 1). The ascending branch that starts from zero field has been referred to as the zero-FORC (Yu & Tauxe, 2005), which has no transient hysteretic magnetization. Transient-free FORCs were measured using such zero-FORCs with the same irregular measurement grid as the remFORC measurements, starting from saturation magnetization and decreasing the field to zero to measure the remanent magnetization and then ramping to the initial reversal field to measure the transient-free magnetization (Zhao et al., 2017). The tFORC is then obtained by subtracting the transient-free FORC from conventional FORC measurements for the same sample. All measurements were made with the same irregular measurement grid, and results were processed using the same data

Table 1
Characteristic Features of Different Magnetic Domain States in FORC-Type Diagrams

	Features on FORC-type diagrams			
Magnetic domain state	FORC	remFORC	iFORC	tFORC
SP		Vertical distribution along the $B_i < 0$ axis.		
SD	Closed positive contours along the B_c axis; negative peak near the lower B_i xis.		Negative-positive-negative triple peak between the $B_i < 0$ and $B_c > 0$ axes.	
Vortex			Pair of negative-positive peaks between the $B_i < 0$ and $B_c > 0$ axes.	Upper and lower lobes and possible butterfly pattern.
MD	Vertical distribution or diverging distribution toward both the positive and negative B_i axis.		Pair of negative-positive peaks between the $B_i < 0$ and $B_c > 0$ axes.	Two wings along the B_i xis.

Note. For more detailed explanations, see text and Zhao et al. (2017).

processing algorithm to enable comparison of results. Finally, an iFORC diagram was calculated by subtracting the transient-free FORC distribution from the remFORC distribution to provide the FORC distribution associated purely with the induced magnetization.

Statistical significance is important for FORC measurements where noise is often large and is amplified by calculation of the second derivative. All FORC-type diagrams presented in this paper are shown with an $\alpha = 0.05$ significance level, which is calculated based on the method of Heslop and Roberts (2012) and indicated by a green dashed line. Significance levels limit interpretation of coercivity and interaction field distributions when FORC features are compromised by measurement noise.

All hysteresis loop and FORC-type measurements were made with a Princeton Measurements Corporation MicroMag 3900 vibrating sample magnetometer (VSM) at the Australian National University. Loose soil and marine sediment samples were packed into pharmaceutical gel caps that were attached to the VSM drive rod. To minimize movement of material and to maximize sample size, the gel caps were filled to maximum capacity and were attached to the drive rod with nonmagnetic glue. For each sample, high-resolution hysteresis loops were measured to 1 T and were used to generate irregular grids for all subsequent FORC-type measurements using the xFORC software (https://sites.google.com/site/irregularforc/) of (Zhao et al., 2017). One hundred and twenty FORCs, remFORCs, and transient-free FORCs were measured with an averaging time ranging from 300 to 600 ms to obtain high-quality results. All data were processed using xFORC with SF of 3 or 4, depending on the signal-to-noise level. The full suite of conventional FORC, remFORC, and transient-free FORC measurements took about 20 hours per sample so that the data presented here represent about 1 month of VSM measurement time. We consider the information obtained to be of sufficient value to justify the long measurement time required.

2.2. Interpretational Framework for FORC, remFORC, iFORC, and tFORC Diagrams

The interpretational framework for conventional FORC diagrams is discussed in detail by Roberts et al. (2014). However, the additional remFORC, iFORC, and tFORC diagrams have unique advantages in distinguishing domain states in samples with complex magnetic mineral mixtures (Zhao et al., 2017). Below, we provide an integrated interpretational framework for identifying each domain state from these four types of FORC diagram. Diagnostic features associated with the SP, stable SD, vortex, and MD states in FORC, remFORC, iFORC, and tFORC diagrams are summarized in Table 1 and Figure 2.

2.2.1. Single-Domain Behavior

As illustrated in Figure 2a, SD particle systems can be represented by a dominant positive region along the B_c axis that corresponds to the coercivity in FORC and remFORC diagrams (Egli, 2006; Muxworthy & Williams, 2005; Pike et al., 1999; Roberts et al., 2014; Zhao et al., 2017). In reality, the coercivity of SD particles in natural samples has a distribution rather than a single value. Therefore, SD behavior in natural samples is represented by elongated or rounded positive distributions along the B_c axis in both FORC and remFORC diagrams, which indicate the coercivity distribution. Non-interacting SD particles, such as magnetite magnetofossils, produce

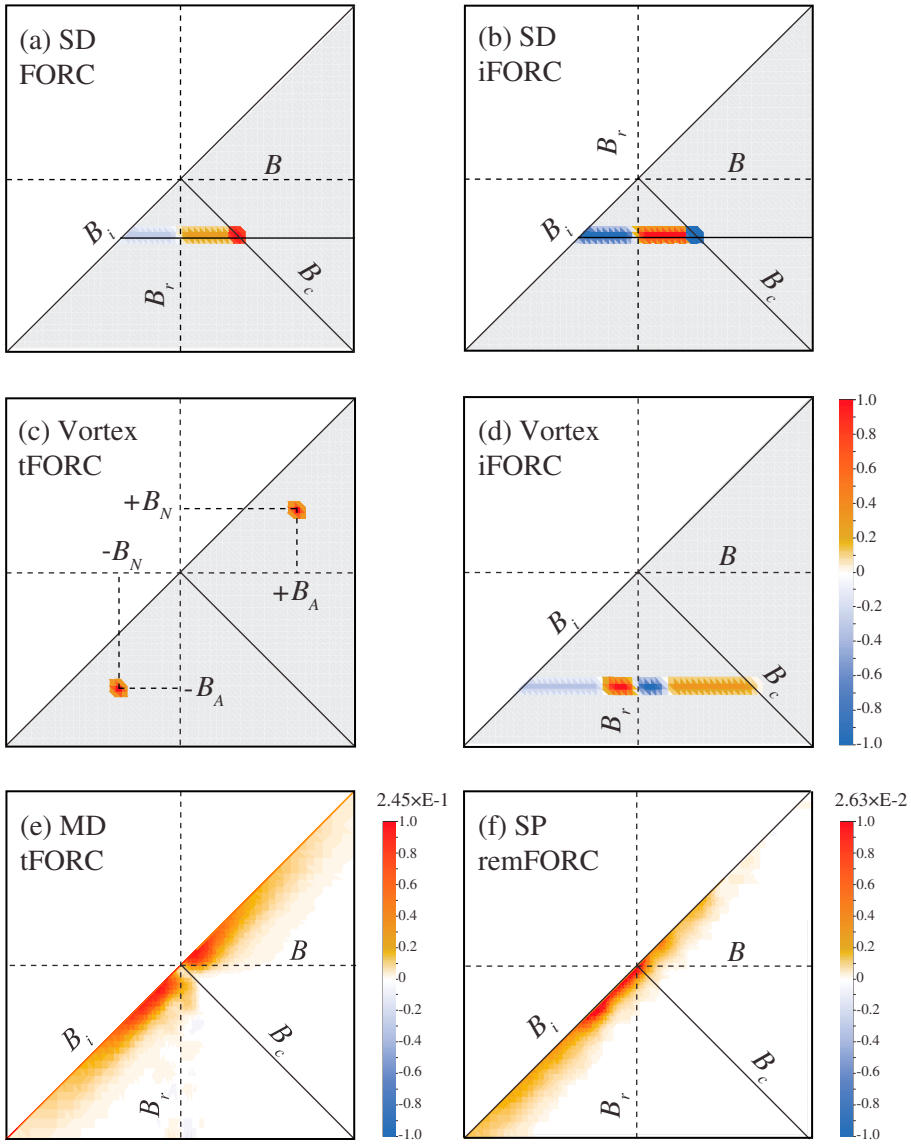

Figure 2. Schematic illustration of the manifestations of each magnetic domain state on the FORC-type diagrams used in this study. (a) Single domain (SD) behavior in a conventional first-order reversal curve (FORC) diagram, with a positive distribution on the B_c axis and a secondary negative peak close to the $B_i < 0$ axis. (b) Characteristic triple negative-positive-negative pattern for SD particles in an induced FORC diagram. (c) Vortex state particles produce a positive peak in both the upper and lower half-planes, where the distance of the peaks from the B_c axis is a measure of the strength of the vortex nucleation and annihilation fields, B_N and B_A, respectively, and their distance from the B_i axis is a measure of coercivity. The two characteristic positive peaks are most clearly evident in transient FORC diagrams. (d) Characteristic negative-positive-negative-positive pattern for vortex behavior in an induced FORC diagram. (e) Transient FORC diagram of a multiple domain (MD) magnetite sample (Zhao et al., 2017). When domain walls start to nucleate within a coarse particle, the two positive peaks due to a vortex state in tFORC diagrams move toward zero on the B_i axis, where domain wall nucleation and annihilation field distributions produce the illustrated "wing" features. (f) RemFORC diagram for superparamagnetic (SP) hematite (sample HGL30; Jiang et al., 2012). SP behavior is manifested as a positive region along the $B_i < 0$ axis.

a ridge-like distribution along the B_c axis with almost no spread along the B_i axis in FORC and remFORC diagrams, which is referred to as a 'central ridge' (Egli et al., 2010). Magnetostatic interactions, however, give rise to spreading along the $B_i = 0$ axis in both FORC and remFORC diagrams, such as in closely packed industrially produced magnetic recording media, and in diagenetic greigite or pyrrhotite samples (Roberts et al., 2006, 2014; Zhao et al., 2017). A subsidiary negative peak near the lower B_i axis (Figure 2a) is a common feature observed for uniaxial SD particles (Muxworthy et al., 2004; Newell, 2005), which is always

absent in remFORC diagrams (Zhao et al., 2017). It is expected that magnetic moments will be oriented randomly in geological samples, so that perfect alignment of the field with the easy axis of magnetization does not occur for all particles. Particles with easy axes that are not aligned parallel to the field will contribute to the negative region on FORC diagrams when the field changes from the upper to the lower curve ($B < 0$). This behavior is associated with a bifurcation at which a stable state and an energy barrier converge and annihilate each other (Newell, 2005). In coarser particles, large jumps are canceled by small jumps due to domain wall movements, so that only positive contributions are seen (Newell, 2005), which makes the negative peak a unique signature of uniaxial SD particles (Figure 2a). The SD particle signature is represented by a triple peak feature in iFORC diagrams (Figure 2b), with a negative peak close to the $B_i < 0$ axis, a positive peak below the B_c axis, and another negative peak above the B_c axis with a slightly higher B_c value. This behavior is caused by the induced magnetization, which is known as an apparent reversible magnetization, when SD particles are oriented at an angle with respect to the applied field. Detailed explanations of this effect are given by Bodale et al., (2011), Della Torre (1999), and Zhao et al. (2017).

2.2.2. Vortex State and Multidomain Behavior

As particles grow larger, the uniform magnetization of SD particles becomes energetically unfavorable. To minimize energy, neighboring spins start to diverge from strict parallelism, and the magnetization fans or curls into the flower or vortex states (Schabes & Bertram, 1988). Eventually, spins organize themselves into regions with quasi-uniform magnetization separated by domain walls to create MD particles. Unlike SD particles, which do not have transient hysteresis, vortex state and MD particles have transient hysteresis due to internal self-demagnetization. Therefore, tFORC diagrams are ideal for characterizing the vortex and MD states (Roberts et al., 2017; Zhao et al., 2017). There is a nucleation field at which the flower state disappears and the vortex state forms, and an annihilation field at which the vortex state disappears. The hysteresis behavior of particles in the magnetic vortex state is often described using simplified hysteron-like loops or modifications thereof that are split into two parts at vortex nucleation B_N and annihilation B_A fields, which give rise to two positive peaks above and below the B_c axis in a tFORC diagram (Figure 2c) (Pike & Fernandez, 1999). A butterfly-shaped feature can be observed in tFORC diagrams if the sample has different vortex nucleation and annihilation fields (Pike & Fernandez, 1999), which provides a direct indication of the presence of vortex state particles. With increasing particle size, both B_N and B_A decrease and the difference between them also decreases (Novosad et al., 2001) and the two positive peaks move toward both the B_i and B_c axes of a tFORC diagram. When discrete peaks are no longer visible in the upper and lower parts of a tFORC diagram, the sample is dominated by MD behavior to produce two (upper and lower) wings (Figure 2e) due to transient hysteresis effects that indicate domain wall nucleation and annihilation field distributions (Pike et al., 2001). The induced magnetization depends on the applied external field strength and magnetization state. In micromagnetic simulations, particles in the vortex and MD states can be approximated by goose-necked hysteresis loops (Goiriena-Goikoetxea et al., 2016), which produce a negative-positive-negative-positive pattern between the $B_i < 0$ axis and the positive $B_c > 0$ axis in iFORC diagrams (Figure 2d).

2.2.3. Superparamagnetism

Thermal fluctuations cause random magnetic moment direction changes in superparamagnetic (SP) particles. SP particles align easily with an external field and give rise to completely reversible hysteresis loops. Theoretically, reversible magnetizations should not make a contribution on a FORC diagram because the mixed second derivative will be zero. However, FORC measurements are made rapidly so that particles with volumes near the SP/SD threshold size produce hysteresis loops with slight irreversibility due to thermal relaxation, which give rise to a peak near the origin of a FORC diagram and a nearly vertical distribution below the $B_c = 0$ axis (Figure 2f) (Pike et al., 2001). In conventional FORC diagrams, this signal is often obscured by the strong negative peak due to uniaxial SD particles or by the large nucleation/annihilation field distributions due to vortex state and MD particles. Thus, remFORC diagrams are particularly useful for isolating SP signals because other signals that contribute to the lower right-hand side of the diagrams are eliminated, which makes the vertical distribution below the $B_c = 0$ axis a unique characteristic of SP particles (Zhao et al., 2017).

2.3. Soil and Marine Sediment Samples

2.3.1. Australian Soils

Australian soils provide a variety of magnetic minerals for testing the FORC-based magnetic domain state diagnosis methods outlined above. Australian soils are distributed over a continent with an area of nearly

Table 2
Detailed Information for Australian Soil Samples Used in This Paper

Sample	Soil type[a]	Lat.[b]	Long.[b]	Geology region[a]	Surface geology[c]	Climate[d]	Relief[a]	Land use[a]
217	Kandosol	−32.315	116.185	Yilgarn Region, Western Australia	Ferruginous duricrust	Temperate, distinctly dry, and hot ummer	157	Nature conservation
GA1069	Kandosol	−15.611	132.625	Daly River Region, Northern Territory	Alluvium	Tropical, rain forest, and monsoonal	66	Grazing native vegetation
GA1086	Kandosol	−24.750	116.260	Gascoyne Region, Western Australia	Durlacher Supersuite	Grassland, hot, and summer drought	85	Grazing native vegetation
GA399	Calcarosol	−28.429	136.847	Eromanga Region, Southern Australia	Colluvium	Desert, hot, and persistently dry	91	Grazing native vegetation
GA857	Calcarosol	−33.540	139.702	Murray Region, Southern Australia	Pooraka Formation	Grassland, warm, and persistently dry	88	Grazing native vegetation
5564	Organosol	−17.365	145.951	Cairns Region, Queensland	Alluvium	Tropical, rain forest, and persistently wet	81	Grazing modified pastures
GA329	Ferrosol	−41.080	145.924	Dundas Region, Tasmania	Oonah Formation	Temperate, no dry season, and mild summer	204	Minimal use
GA521	Tenosol	−19.997	146.434	Charters Region, Queensland	Lavery Creek Granite	Grassland, hot, and winter drought	140	Grazing native vegetation
11621	Vertosol	−23.723	148.118	Bowen Region, Queensland	Mafic volcanic rocks	Subtropical and moderately dry winter	126	Dryland cropping
GA533	Dermosol	−38.088	144.279	Otway Region, Victoria	Alluvium	Temperate, no dry season, andwarm ummer	167	Dryland cropping

[a]Australian Soil Classification, Geology region, relief and land use data are extracted from Australian Soil Resource Information System (http://www.asris.csiro.au/mapping/viewer.htm?). [b]Lat. and Long. represent latitude and longitude, respectively. [c]Surface geology information is extracted from Raymond et al. (2012). [d]Climate zone information is extracted from Climate classification maps, Australian Government, Bureau of Meteorology, based on a modified Köppen classification system and a standard 30 year climatology (1961–1990). http://www.bom.gov.au/jsp/ncc/climate_averages/climate-classifications/index.jsp?maptype = kpn#maps.

7,800,000 km^2, of which approximately one third lies within the tropics. The soils have developed on a range of rock types and under climatic conditions that vary from the alpine zones of southeastern Australia and Tasmania, to the Mediterranean zones of southern and southwestern Australia, the wet and dry tropics of Queensland and the Northern Territory, to the low rainfall, desert areas in the center. Fifty out of 500 samples were selected for detailed FORC measurements based on their magnetic properties (susceptibility, hysteresis loops, and coercivity), soil classification, and parent materials. For this study, results for 10 samples from 7 soil orders (Isbell, 2002) are used. The samples come from different sources, mainly the Australian Commonwealth Scientific and Industrial Research Organization National Soil Archive and National Geochemical Survey of Australia (see Viscarra Rossel et al., 2010, for details). Information concerning soil development for the presented samples is listed in Table 2.

2.3.2. Chinese Loess and Paleosols

Chinese loess-paleosol sequences are a key archive for reconstructing monsoon evolution, aridification history, and abrupt climate change (Maher, 2016; Porter & An, 1995). Environmental magnetism has proven to be one of the most important research methods for investigating paleoclimate changes recorded in loess deposits (Deng et al., 2005; Evans & Heller, 2003; Hu et al., 2015; Liu et al., 2007). Thus, analysis of the magnetic properties of loess/paleosol samples is crucial for building an interpretational framework to determine the paleoclimate significance of magnetic properties. We analyzed two pairs of loess/paleosol samples from the well-known Baicaoyuan and Ganzi sections. The Baicaoyuan section is located on the western Chinese Loess Plateau (CLP), where an arid/semiarid continental climate dominates. The Ganzi section is located on the southeastern Tibetan Plateau (TP), where a monsoon-influenced humid continental climate and subarctic climate dominates. The Ganzi loess has a different source area and more SP particles compared to CLP loess sections, while coarse lithogenic magnetite dominates the Baicaoyuan loess (Deng, 2008). These differences are useful for assessing the new FORC diagnosis methods. Two samples from the last glacial loess (L1) and last-interglacial paleosol (S1) at Baicaoyuan were analyzed along with two samples from L1 and the Holocene paleosol (S0) from Ganzi.

2.3.3. Marine Sediments

Marine sediments contain magnetic minerals with mixed detrital, biogenic, and diagenetic origins (Roberts, 2015) that produce distinctive behavior in conventional FORC diagrams (Chang et al., 2014). We analyzed two

marine sediment samples to illustrate the value of the additional FORC-type diagrams for understanding mixed magnetic signals. Sample PC710 is from pelagic biogenic carbonate (mainly nannofossil and foraminiferal) ooze from Ocean Drilling Program Site 710B, western equatorial Indian Ocean (04°18.7′S, 60°58.8′E, 3824.3 m water depth), where magnetofossils contribute significantly to the magnetization. Sample DE769 is from Ocean Drilling Program Site 769B, from a bathymetric high on Cagayan Ridge, Sulu Sea (08°47.12′N, 121°17.68′E, 3643.6 water depth). The sample is from Unit I at the depth of 62.82 mbsf, where the dominant lithology is a mixture of pelagic biogenic carbonate and hemipelagic clay (Rangin et al., 1990).

3. Results

3.1. Australian Soils

3.1.1. Calcarosols

As their name suggests, calcarosols contain abundant amounts of calcium carbonate. Samples GA857 and GA399 are both from South Australia and developed on colluvium and poorly sorted clayey sand, respectively. The FORC diagram for sample GA857 has a positive peak at $B_c \approx 10$ mT, with distributed coercivities along the B_c axis and spreading parallel to the B_i axis, which is suggestive of "pseudo-single domain" (PSD) behavior (Figure 3a). Such a small B_c value indicates the presence of a low coercivity ferrimagnetic component, most likely magnetite or maghemite. Sample GA399 has similar behavior in a FORC diagram with lower coercivity and a "PSD"-like feature and spreading of the FORC distribution along the B_i axis (Figure 3e). A small positive region along the $B_i < 0$ axis is also evident in both samples, which is indicative of thermal relaxation of SP particles (see section 2.2.3). GA399 has a significant high coercivity component (Figures 3a and 3e) that is more clearly evident in a remFORC diagram (Figure 3f). The coercivity of this component extends to >800 mT, which, along with the bright red color of the sample, indicates that hematite is present. RemFORC diagrams also illustrate more effectively the contribution of SP particles (Figures 3b and 3f). Induced FORC diagrams contain the characteristic negative-positive-negative-positive pattern that reflects vortex behavior (Figures 3c and 3g). In tFORC diagrams (Figures 3d and 3h), two positive peaks occur in the upper right-hand and lower left-hand regions, respectively, which are characteristic of vortex state particles. Thus, the range of FORC-type diagrams demonstrates the dominance of particles in the vortex state along with SD hematite for GA399 and a mixture of SD and vortex state particles for GA857.

The conventional FORC diagrams in Figures 3a and 3e are typical of geological PSD materials. However, when using the additional types of FORC diagrams presented in Figure 3, the nature of the magnetic domain states present in the samples is identified more clearly. The mixture of ferrimagnetic particles in the SD, SP, and vortex states, together with hematite, is demonstrated clearly, whereas an ambiguous PSD determination is likely to be made on the basis of a conventional FORC diagram alone (see also Roberts et al., 2017). Calcarosols have variable properties over short distances due to substantial eolian contributions along with wetting/drying soil formation processes. Thus, they contain multiple magnetic mineral sources, as reflected in the complex mixture of magnetic particle types indicated in the FORC diagrams in Figure 3.

3.1.2. Kandosols

Kandosols lack strong textural contrasts and are not calcareous throughout. We analyzed three kandosol samples from Western Australia (samples GA1086 and 217) and the Northern Territory (sample GA1069). GA1086 is from the Gascoyne Province near the tungsten-magnetite skarns at Nardoo Well. The FORC diagram for GA1086 is indicative of typical MD behavior with a widely divergent and nearly symmetrical distribution along the B_i axis with a small tail on the B_c axis (Figure 4a). The tFORC diagram has characteristic wings along the B_i axis, which indicate dominantly MD behavior (Figure 4d). The negative-positive-negative-positive pattern in the iFORC diagram (Figure 4c) is also consistent with MD behavior. The narrow positive distribution along the $B_i < 0$ axis in the remFORC diagram indicates the presence of SP particles, probably produced by pedogenesis, and the positive distribution along the B_c axis in the remFORC diagram is indicative of the remanence-bearing MD fraction (Figure 4b).

Sample GA1069 is from the Daly River region, Northern Territory, where a tropical rain forest climate is dominant. Warm and wet climates favor formation of fine pedogenic magnetite and maghemite and hematite. Unlike GA1086, in which coarse magnetite is the main magnetic mineral, GA1069 has a significant SP and hematite contribution, as evident in both FORC and remFORC diagrams (Figures 4e and 4f). The coercivity distribution extends to >1,000 mT, which indicates contributions from hematite and goethite (Figure 4f).

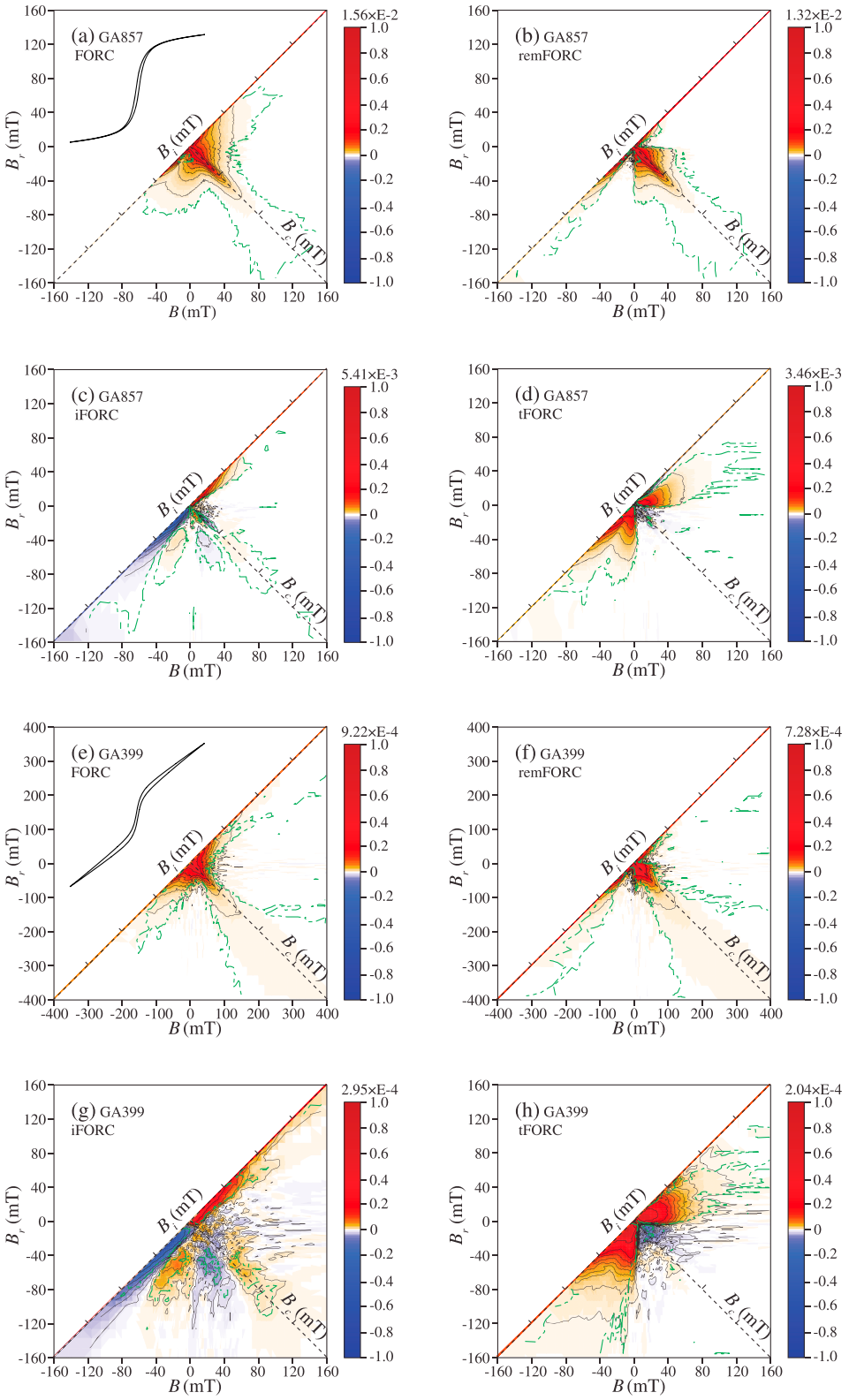

Figure 3. First-order reversal curve (FORC) results for two calcarosol samples GA857 and GA399, which were measured to a maximum field of 300 mT and 1 T, respectively. Plots are restricted to a lower field for clarity. (a, e) Conventional FORC diagrams, (b, f) remanent FORC diagrams, (c, g) induced FORC diagrams, and (d, h) transient FORC diagrams. Smoothing factor = 3 for all diagrams; 120 FORCs were measured with 300 ms averaging time. Saturation fields for the hysteresis loops in Figures 3a and 3e are 300 mT and 1 T, respectively.

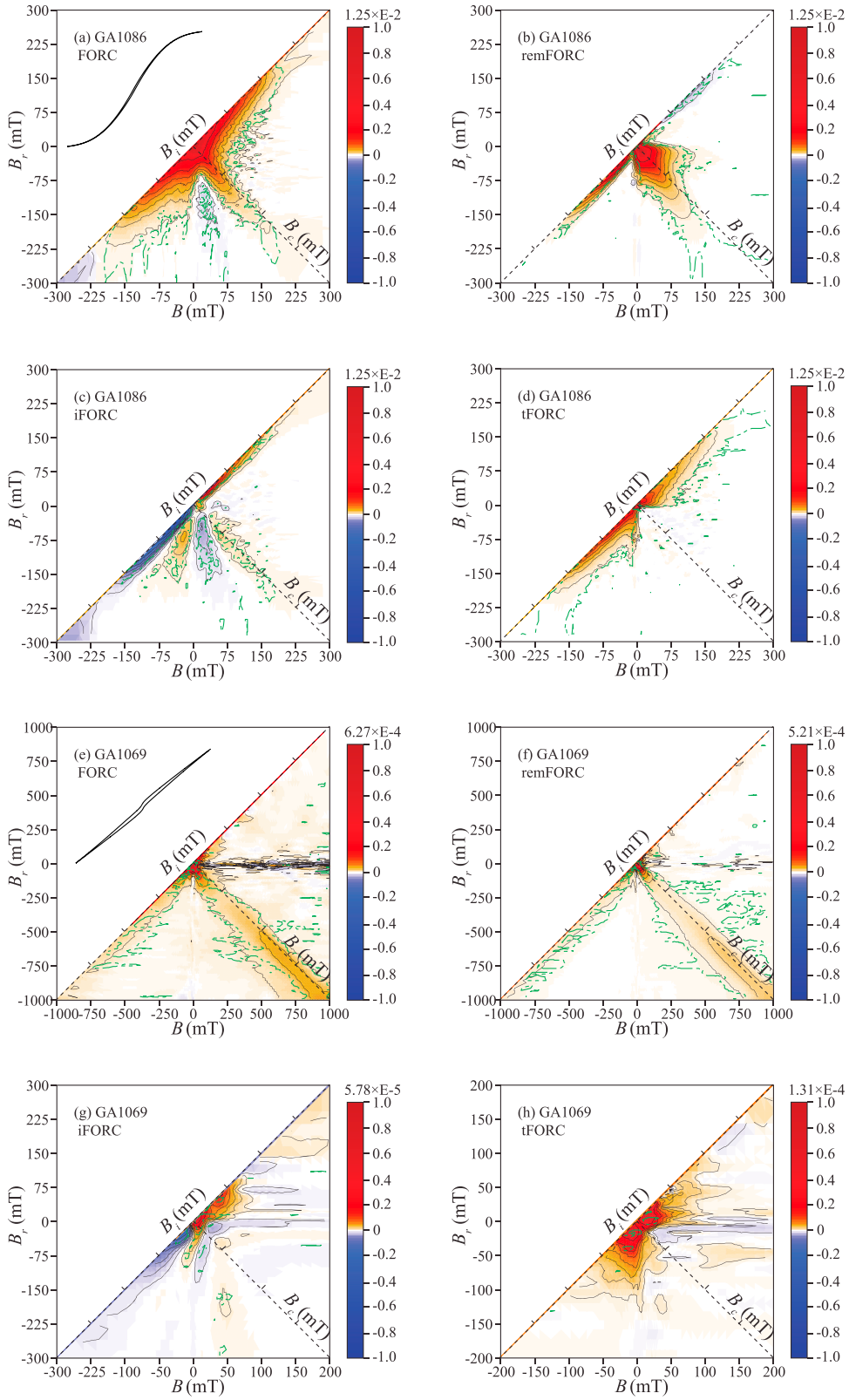

Figure 4. First-order reversal curve (FORC) results for two kandosol samples (GA1086 and GA1069). (a, e) Conventional FORC diagrams, (b, f) remanent FORC diagrams, (c, g) induced FORC diagrams, and (d, h) transient FORC diagrams. Smoothing factor SF = 3 for all diagrams for GA1086 and smoothing factor = 4 for sample GA1069; 120 FORCs were measured with 300 ms averaging time. Saturation fields for the hysteresis loops in Figures 4a and 4e are 300 mT and 1 T, respectively.

The negative-positive-negative-positive feature in the iFORC diagram (Figure 4g) and the upper and lower lobes in the tFORC diagram (Figure 4h) indicate an additional contribution from vortex state particles.

Sample 217 is a ferruginous duricrust with high Fe oxide concentrations from the Yilgarn Region, Western Australia. The FORC diagram is indicative of typical SD behavior, with a positive B_c peak at about 40 mT and a negative region close to the $B_i < 0$ axis (Figure 5a). A characteristic triple negative-positive-negative feature is also evident in the iFORC diagram (Figure 5c), which provides further evidence for dominantly SD behavior. The green significance level line indicates a high coercivity contribution (>300 mT) from hematite or goethite (Figures 5a and 5b). A positive region along the $B_i < 0$ axis in the remFORC diagram indicates the presence of SP particles. The tFORC diagram includes upper and lower lobes with a slightly larger positive region along the $B_i < 0$ axis, which indicates the presence of vortex state particles (Figure 5d). Although SD particles dominate sample 217, the presence of SP and vortex state particles becomes evident when using multiple FORC-type diagrams.

3.1.3. Organosols

Organosols are dominated by organic material, and are distributed mainly in wet tropical to alpine regions, and usually form over small areas. Sample 5564 is from the Cairns Region, which has a persistently wet tropical rain forest climate. FORC and remFORC diagrams for sample 5564 indicate dominantly SD behavior with an elongated coercivity distribution that extends to >300 mT, which suggests a mixture of ferrimagnetic and antiferromagnetic components (Figures 5e and 5f). There is virtually no positive region along the $B_i < 0$ axis of the remFORC diagram, which indicates a negligible contribution from SP particles. The iFORC diagram has a weak triple negative-positive-negative pattern that confirms the dominant SD behavior. Upper and lower lobes in the tFORC diagram are indicative of vortex state particles.

3.1.4. Ferrosols and Tenosols

Ferrosols have high free iron oxide contents and lack a strong textural contrast. These soils form almost entirely on either basic or ultrabasic igneous rocks or alluvium derived therefrom. These soils occur mainly in mountainous parts of northwestern and eastern Tasmania. Tenosols have weak pedologic development and are widespread in many parts of Australia, particularly in the center and west. Sample GA329 is a ferrosol from the Dundas Region, Tasmania, and sample GA521 is a tenosol from the Charters Region, Queensland. For both samples, FORC diagrams have a typical PSD distribution with significant divergence along the B_i axis (Figures 6a and 6e). The characteristic negative-positive-negative-positive feature on iFORC diagrams (Figures 6c and 6g), and the upper and lower lobes on tFORC diagrams (Figures 6d and 6h) indicate the dominance of vortex state behavior. A positive region close to the $B_i < 0$ axis and a coercivity distribution that extends to 300 mT indicate a contribution from SP and high coercivity particles, respectively.

3.1.5. Vertosols and Dermosols

Vertosols are clay soils with shrink-swell properties that crack when dry. Australia has the greatest areal distribution and diversity of cracking clay soils in the world; vertosols are distributed widely, especially in the eastern lowlands of Australia. Dermosols have structured B2 horizons and lack strong textural contrast. Vertosol sample 11621 and dermosol sample GA533 are from the Bowen Region, Queensland, and the Otway Region, Victoria, respectively. The two samples have similar patterns in all FORC-type diagrams (Figure 7). FORC diagrams have a low coercivity peak and moderate spreading along the B_i axis (Figures 7a and 7e). A small positive tail near the $B_i < 0$ axis in FORC diagrams and a more significant tail in remFORC diagrams (Figures 7b and 7f) reflect the presence of SP particles. SD behavior is represented by the triple negative-positive-negative regions in iFORC diagrams (Figures 7c and 7g). The tFORC diagrams have large positive upper and lower lobes that represent a significant contribution from vortex state particles. Thus, the two samples contain a mixture of SP, SD, and vortex state particles.

3.2. Chinese Loess and Paleosols

Unlike Australian surface soil samples, which contain highly variable magnetic properties, loess and paleosol samples from the CLP and TP have similar behavior in all FORC-type diagrams presented here (Figures 8 and 9). Loess samples from the last glacial have typical PSD features (Muxworthy & Dunlop, 2002; Roberts et al., 2000) as demonstrated by Hu et al. (2015). Using a combination of remFORC, iFORC, and tFORC diagrams, we can further diagnose this ambiguous PSD feature as due to a mixture of SP, SD, and vortex state signals, as indicated by the positive region close to the $B_i < 0$ axis in remFORC diagrams, the negative-positive-negative-positive pattern in iFORC diagrams, and the upper and lower lobes in tFORC

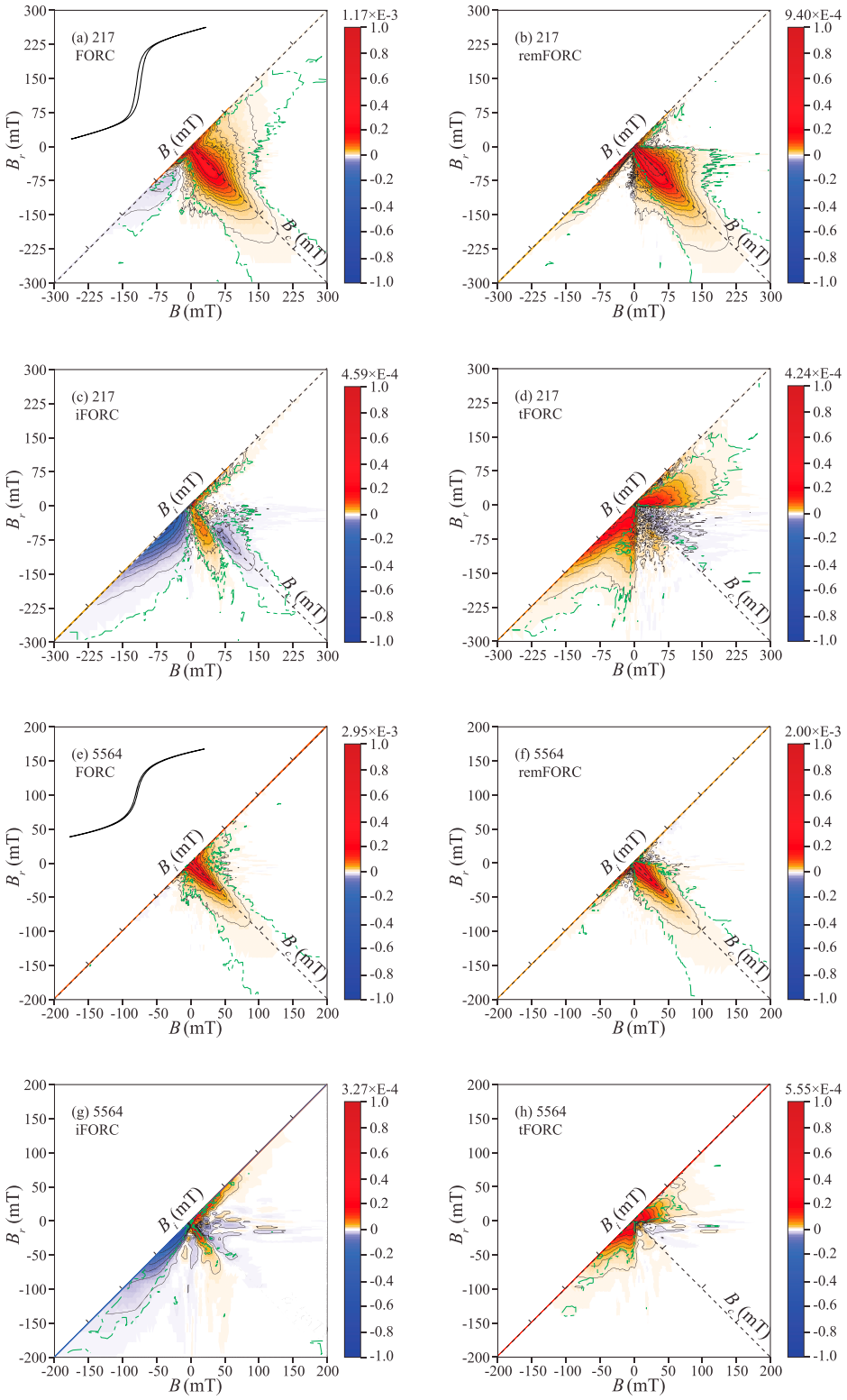

Figure 5. First-order reversal curve (FORC) results for kandosol sample 217 and organosol sample 5564. Measurements were made to a maximum field of 500 mT, but plots are restricted to lower fields for clarity. (a, e) Conventional FORC diagrams, (b, f) remanent FORC diagrams, (c, g) induced FORC diagrams, and (d, h) transient FORC diagrams. Smoothing factor SF = 3 for 217, and for FORC and remFORC diagrams for 5564. Smoothing factor = 4 for the iFORC and tFORC diagrams for 5564. The 120 FORCs were measured with averaging time of 200 ms for sample 217 and 500 ms for sample 5564. Saturation fields for the hysteresis loops in Figures 5a and 5e are 1 T and 400 mT, respectively.

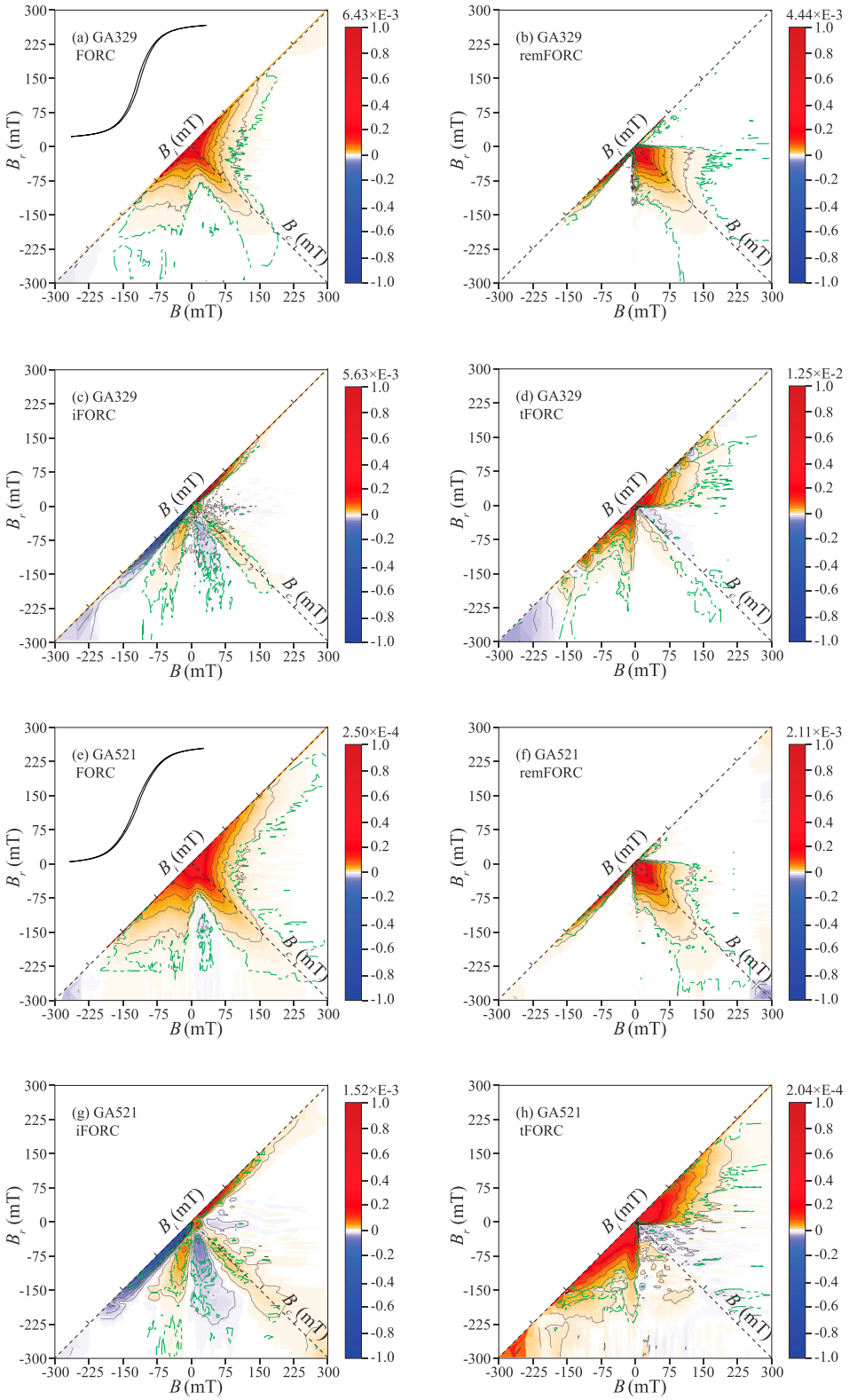

Figure 6. First-order reversal curve (FORC) results for ferrosol (GA329) and tenosol (GA521) samples. (a, e) Conventional FORC diagrams, (b, f) remanent FORC diagrams, (c, g) induced FORC diagrams, and (d, h) transient FORC diagrams. Smoothing factor = 3 for GA329, and for the FORC and remFORC diagrams for GA521. Smoothing factor = 4 for the iFORC and tFORC diagrams for GA521. The 120 FORCs were measured with 300 ms averaging time. Saturation fields for the hysteresis loops in Figures 6a and 6e are 400 mT.

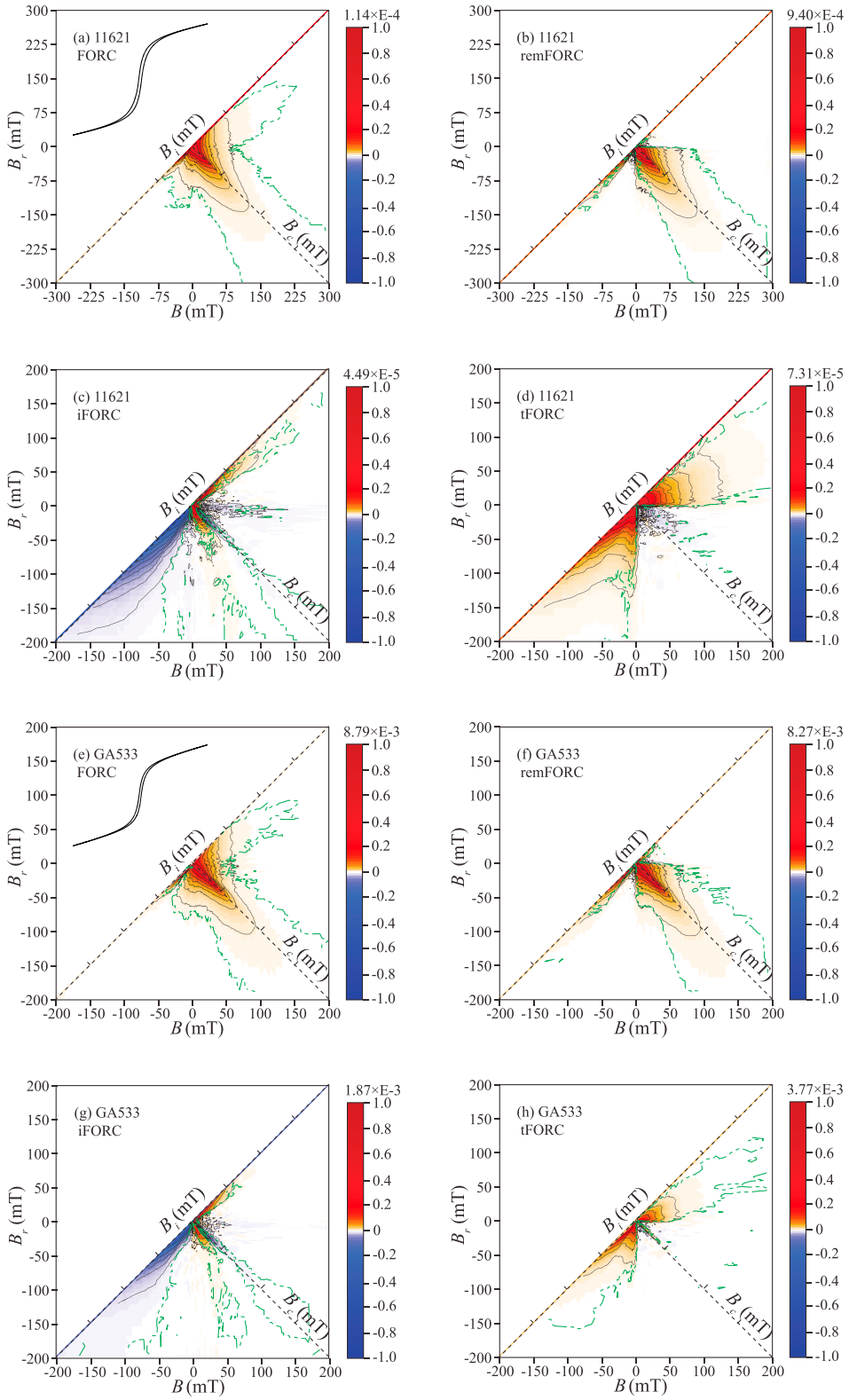

Figure 7. First-order reversal curve (FORC) results for vertosol (11621) and dermosol (GA533) samples. (a, e) Conventional FORC diagrams, (b, f) remanent FORC diagrams, (c, g) induced FORC diagrams, and (d, h) transient FORC diagrams. Smoothing factor = 3 for the FORC and remFORC diagrams and smoothing factor = 4 for the iFORC and tFORC diagrams; 120 FORCs were measured with 500 ms averaging time. Saturation fields for the hysteresis loops in Figures 7a and 7e are 600 mT.

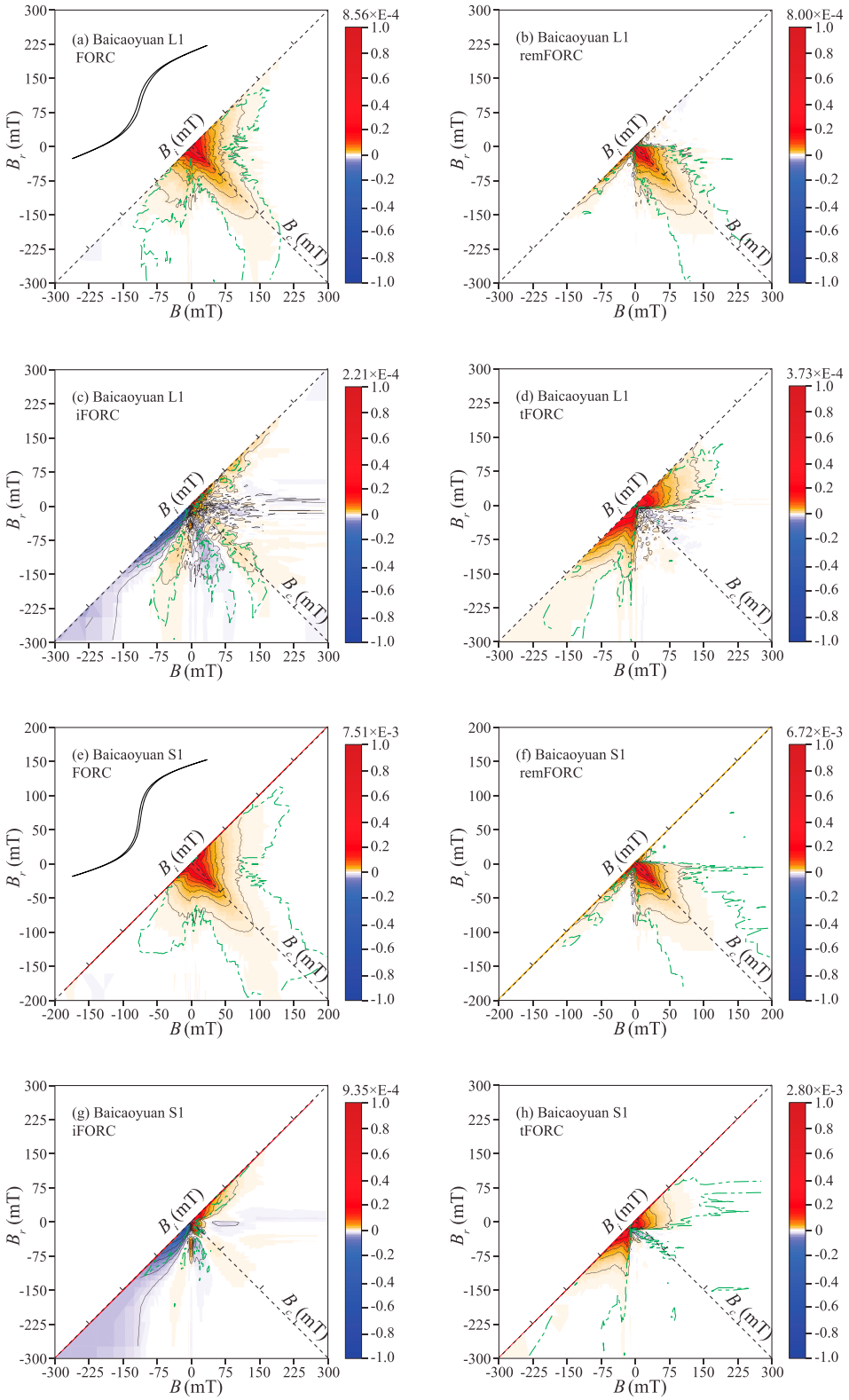

Figure 8. First-order reversal curve (FORC) results for loess and paleosol samples from Baicaoyuan. (a, e) Conventional FORC diagrams, (b, f) remanent FORC diagrams, (c, g) induced FORC diagrams, and (d, h) transient FORC diagrams. Smoothing factor = 3 is used for the FORC and remFORC diagrams and smoothing factor = 4 for the iFORC and tFORC diagrams; 80 FORCs were measured with 200 ms averaging time. Saturation fields for the hysteresis loops in Figures 8a and 8e are 500 mT.

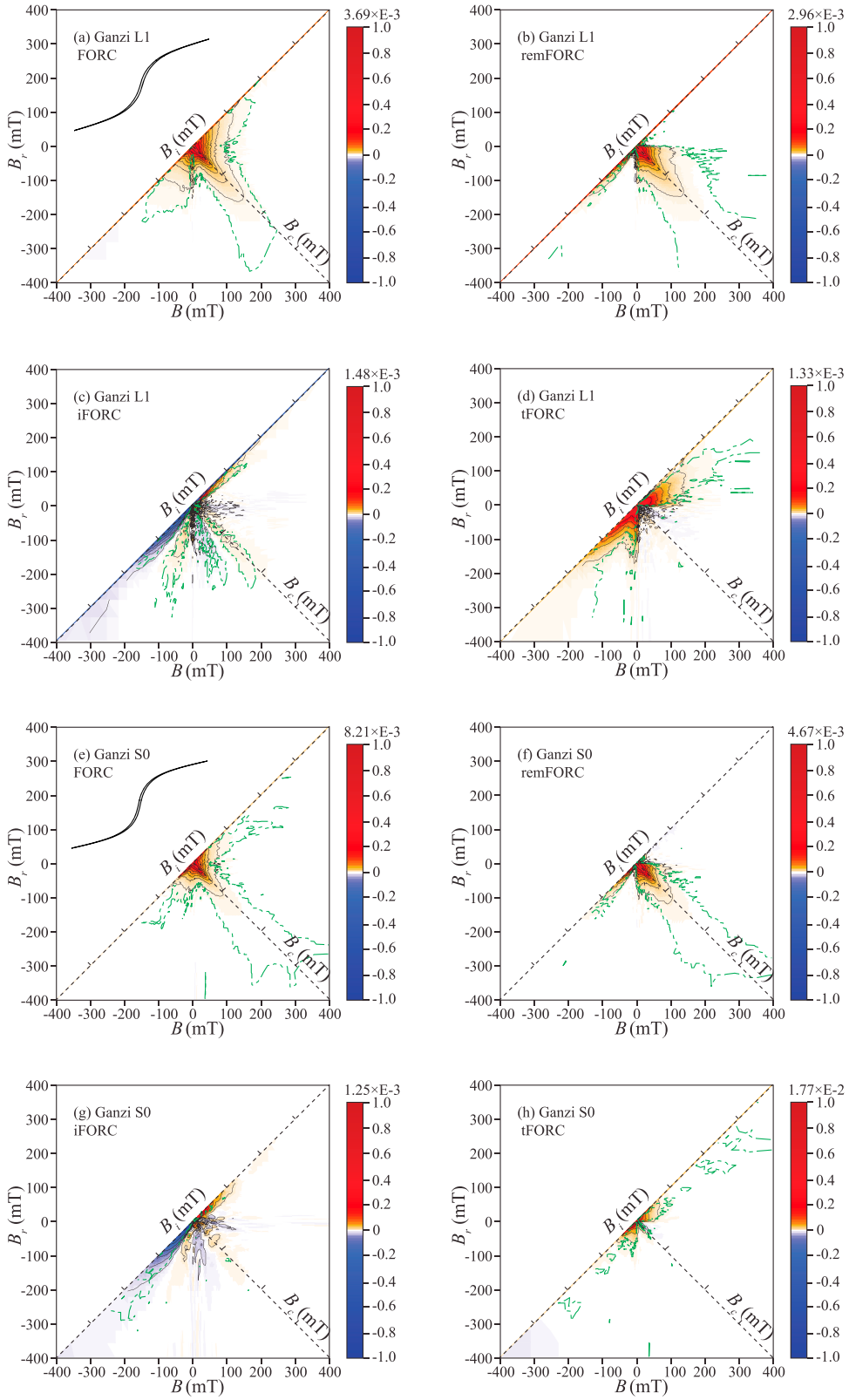

Figure 9. First-order reversal curve (FORC) results for loess and paleosol samples from Ganzi. (a, e) Conventional FORC diagrams, (b, f) remanent FORC diagrams, (c, g) induced FORC diagrams, and (d, h) transient FORC diagrams. Smoothing factor = 3 for the FORC and remFORC diagrams, and smoothing factor = 4 for the iFORC and tFORC diagrams; 120 FORCs were measured with 200 ms averaging time. Saturation fields for the hysteresis loops in Figures 9a and 9e are 500 mT.

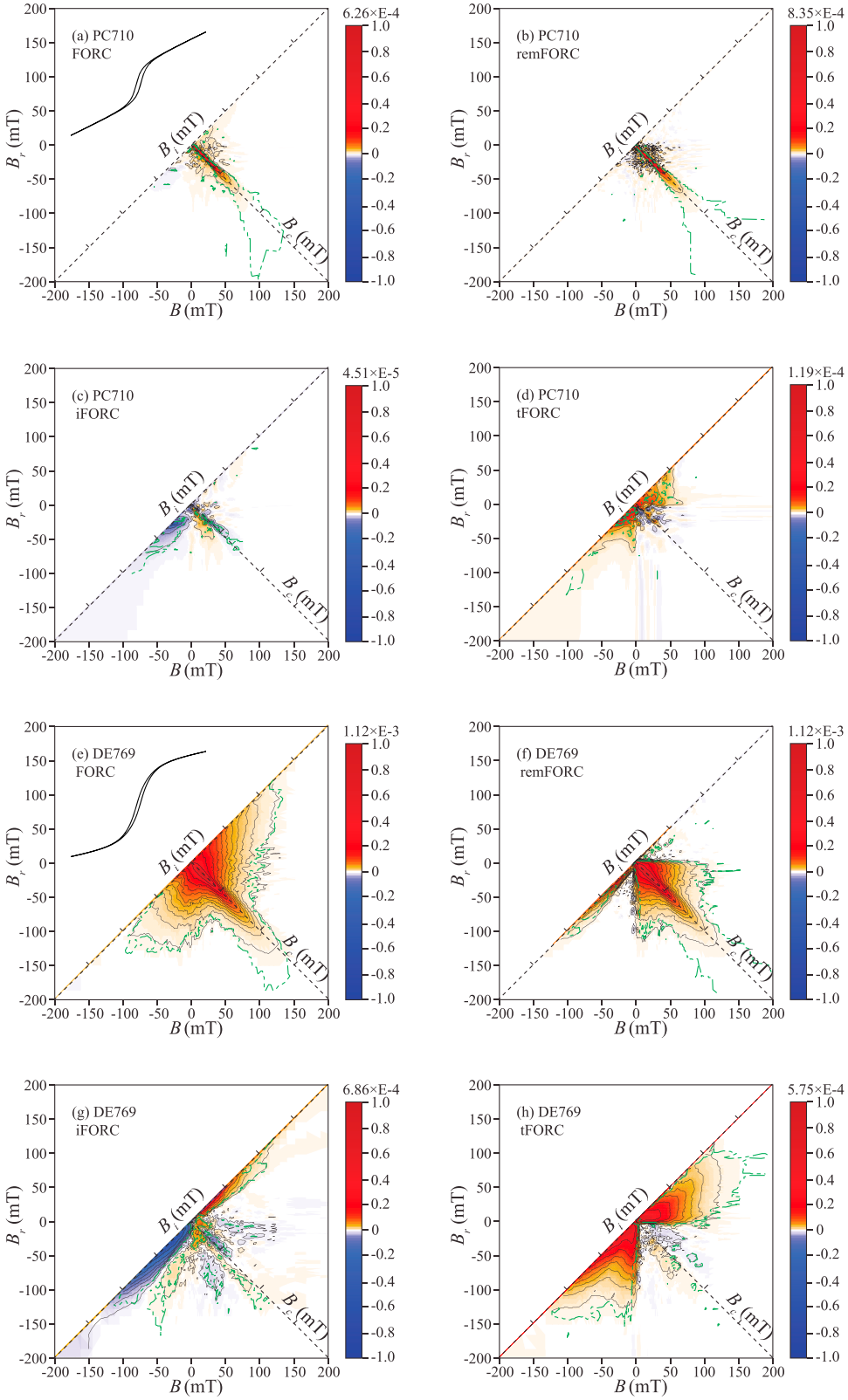

Figure 10. First-order reversal curve (FORC) results for marine sediments from Ocean Drilling Program sites 710 and 769. (a, e) Conventional FORC diagrams, (b, f) remanent FORC diagrams, (c, g) induced FORC diagrams, and (d, h) transient FORC diagrams. Smoothing factor = 4 for PC710 and smoothing factor = 3 for DE769; 120 FORCs were measured with 200 ms average time. Saturation fields for the hysteresis loops in Figures 10a and 10e are 400 mT.

diagrams, respectively (Figures 8b–8d and 9b–9d). Compared to loess samples, paleosols from the last interglacial on the CLP and from the Holocene on the TP have weaker vortex state signals and a stronger SD signal in FORC and iFORC diagrams (Figures 8 and 9), especially for the paleosol from the TP. Interglacial periods on the CLP and TP favor stronger pedogenesis with lower coarser eolian inputs due to a weaker winter monsoon, which results in a larger proportion of pedogenic SD magnetite and/or maghemite and a smaller proportion of larger vortex state particles. The eolian source area on the CLP and TP is different (Ferrat et al., 2011; Hu et al., 2015), so the similar domain state distributions of magnetic minerals in these loess and paleosol samples suggests that the effects of different eolian parent materials have been minimized by mixing during transportation and by similar post-depositional pedogenic processes.

3.3. Marine Sediments

Pelagic carbonates are deposited far from continents, usually at water depths of 3,000–6,000 m, at rates slower than 10 cm/kyr, and with carbonate contents >30% (Roberts et al., 2013). Pelagic carbonates are important for paleomagnetism because they often provide high-fidelity ancient geomagnetic field records. SD magnetofossils can dominate the magnetic properties of pelagic carbonates, which often lack significant terrigenous particle concentrations (Chang et al., 2014; Roberts et al., 2011, 2013). Sample PC710 is a pelagic carbonate from the western equatorial Indian Ocean. A dominant central ridge is evident in both conventional FORC and remFORC diagrams with peak coercivities of about 30 mT (Figures 10a and 10b), which is indicative of SD biogenic magnetite in chains (Egli et al., 2010; Heslop et al., 2013; Larrasoaña et al., 2012; Roberts et al., 2012). The coercivity distribution has a significant tail. The iFORC diagram also indicates dominantly SD behavior with the characteristic triple negative-positive-negative feature (Figure 10c). Upper and lower lobes are moderately well developed in the tFORC diagram (Figure 10d), which suggests the presence of a contribution from probable detrital particles in the vortex state. In contrast, sample DE769 from the Sulu Sea has a significant contribution from larger vortex state particles, as indicated by the large spread along the B_i axis in a conventional FORC diagram (Figure 10e), the negative-positive-negative-positive feature in the iFORC diagram (Figure 10g), and the upper and lower lobes in the tFORC diagram (Figure 10h). A central ridge SD signature is also evident in FORC and remFORC diagrams, and from the triple feature in the iFORC diagram (Figures 10e, 10f, and 10g). We conclude that the studied Sulu Sea sample contains a mixture of detrital and biogenic magnetic minerals, which is consistent with the mixture of pelagic biogenic carbonate and hemipelagic clay in this sample.

4. Discussion

The results presented above provide evidence for how the wider range of FORC-type diagrams of Zhao et al. (2017) enable more precise domain state diagnosis than existing techniques and enhance significantly the information provided by conventional FORC diagrams. Comprehensive domain state diagnosis for mixed magnetic particle assemblages is assisted markedly by the information provided by the other FORC-type diagrams. For example, a conventional FORC diagram for kandosol sample 217 would be interpreted conventionally in terms of a dominantly SD magnetic particle assemblage (Figure 5a). In addition, however, the remFORC diagram provides evidence of significant thermal relaxation in SP particles (Figure 5b) and the tFORC diagram provides evidence for a significant contribution from vortex state particles (Figure 5d). While the additional FORC-type measurements treble the time required for a single conventional FORC measurement, the comprehensive domain state information provided by the expanded suite of FORC-type diagrams is powerful and justifies the extra time required, especially since the measurement procedure is automated (see Zhao et al., 2017, for details). Each FORC-type diagram is scaled according to the maximum magnetization for the respective magnetic component analyzed (see the color scales for each diagram), so that quantitative estimation of the contribution of each component is possible.

FORC diagrams have provided key evidence in recognizing that genuine SD behavior is much more widespread in the geological record than was evident from the dominant PSD determination obtained from hysteresis parameter analysis (Roberts et al., 2012). As is evident from results for most samples analyzed here and as argued by Roberts et al. (2017), SD and vortex state particles are extremely common in nature. The widespread occurrence of vortex state particles should not be surprising because the size range for stable SD behavior in magnetite is narrow (Muxworthy & Williams, 2009), so vortex state behavior should be expected even when particle size distributions are relatively narrow. For example, Zhao et al. (2017) demonstrated that

a magnetic recording medium sample, which would be expected to be optimized for stable SD recording, contains a significant particle fraction in the vortex state. The only samples analyzed here in which vortex states were not detected are dominated by coarse MD particles (Figure 4). We consider it likely that increased use of tFORC diagrams will prove decisive in recognizing the true, and likely significant, contribution of the vortex state in natural magnetic particle assemblages (Roberts et al., 2017).

It is important to consider whether signals in the different FORC-type diagrams are unique or whether they could be produced by multiple magnetic mechanisms. For example, Zhao et al. (2017) and Roberts et al. (2017) discussed potential ambiguity in discriminating coarse vortex state particles from fine MD particles using tFORC diagrams when nucleation and annihilation fields for vortices and domain walls become small. This is likely to remain an issue because of the gradual transition from the vortex to MD states. A more important ambiguity could be produced by magnetofossil chain collapse. When a magnetofossil chain is intact, it produces a strong dipolar magnetic signature (Dunin-Borkowski et al., 1998). When a chain collapses, the magnetic flux associated with individual particles could then link to create a super-vortex-like structure (see Harrison et al., 2002, for images of supervortex structures in strongly interacting magnetite-ulvöspinel lamellae). Such a super-vortex-like structure due to magnetofossil chain collapse would be manifest as a vortex signature in FORC diagrams, as suggested by Egli and Winklhofer (2014) and as simulated by Harrison and Lascu (2014) in their Figures 7c and 7d. Such false positives could be important in marine sediments where magnetite magnetofossils make significant contributions to the magnetization. It remains to be seen whether magnetofossil chain collapse can cause the vortex signatures shown in Figure 10d. However, magnetotactic bacteria are aquatic organisms (e.g., Frankel & Bazylinski, 2005) and are unlikely to occur in nonaquatic soil environments, particularly in arid climates. This is a significant reason for our focus on Australian soil samples. Thus, our widespread identification of magnetic vortex state particles is considered to be real. Based on our results, we conclude that coarse lithogenic magnetic particles occur commonly in the magnetic vortex state and that this state should not be considered "exotic" (e.g., Dunlop, 2002). Overall, both intraparticle and super-vortex states are likely to produce similar magnetic signals that are equivalently important in paleomagnetism. The widespread nature of these signals has likely been underrecognized. Routine use of the methods used here should help to redress this imbalance and provide a more realistic assessment of the prevalence of vortex states in natural samples.

Finally, the FORC diagrams presented here were produced with user-adjustable nonlinear color scales. This, combined with use of significance levels defined following Heslop and Roberts (2012), maximizes the visibility of responses due to minerals with weak magnetic moments such as hematite (Figures 3f, 4f, 5b, 5f, 6b, 7b, 8b, 9b, 9f, 10b, and 10f). A high coercivity component is detected in most samples analyzed here, which is consistent with the expectation that hematite occurs commonly in geological samples. Our approach overcomes a long-known weakness of FORC diagrams, where significant concentrations of materials with weak spontaneous magnetization like hematite are invisible in FORC diagrams when modest concentrations of materials with strong spontaneous magnetization like magnetite are also present (e.g., Muxworthy et al., 2005; Roberts et al., 2014). Detecting and quantifying the full magnetic particle assemblage is critical in many magnetic applications, and the approach used here should help in developing a more quantitative approach to FORC diagram analysis.

5. Conclusions

We present the first detailed results for an additional set of FORC-type diagrams for diverse soil, loess/paleosol, and marine sediment samples. Our results demonstrate that the wider range of information provided by these additional measurements, which relate specifically to remanent, induced, and transient magnetizations, is diagnostically powerful and assists greatly in magnetic domain state diagnosis in geological samples. While the additional FORC-type measurements take approximately 3 times longer to measure than conventional FORC measurements alone, the measurements are automated, and the diagnostic value of the information provided adds value, particularly for geological samples that contain complex mixtures of magnetic minerals and domain states. From our diverse set of samples, transient FORC diagrams enable identification of magnetic vortex state particles in all but the coarsest samples analyzed. It is likely, therefore, that vortex state particles will be identified routinely in the geological record and that this state should not be considered exotic. Remanent FORC diagrams also provide important information about the domain state of the remanence-bearing magnetic mineral fraction, which is fundamental to paleomagnetic recording.

Acknowledgments
This work was supported financially by the Australian Research Council (grant DP160100805). All data used to produce the figures that have not been previously published will be uploaded into the PANGAEA database portal (http://doi.pangaea.de) prior to publication.

References

Bodale, I., Stoleriu, L., & Stancu, A. (2011). Reversible and irreversible components evaluation in hysteretic processes using first and second-order magnetization curves. *IEEE Transactions on Magnetics*, *47*, 192–197. https://doi.org/10.1109/tmag.2010.2083679

Chang, L., Roberts, A. P., Winklhofer, M., Heslop, D., Dekkers, M. J., Krijgsman, W., et al. (2014). Magnetic detection and characterization of biogenic magnetic minerals: A comparison of ferromagnetic resonance and first-order reversal curve diagrams. *Journal of Geophysical Research: Solid Earth*, *119*, 6136–6158. https://doi.org/10.1002/2014JB011213

Channell, J. E. T., Harrison, R. J., Lascu, I., McCave, I. N., Hibbert, F. D., & Austin, W. E. N. (2016). Magnetic record of deglaciation using FORC-PCA, sortable-silt grain size, and magnetic excursion at 26 ka, from the Rockall Trough (NE Atlantic). *Geochemistry, Geophysics, Geosystems*, *17*, 1823–1841. https://doi.org/10.1002/2016gc006300

Della Torre, E. (1999). *Magnetic Hysteresis*. Piscataway, NJ: IEEE Press.

Deng, C. L. (2008). Paleomagnetic and mineral magnetic investigation of the Baicaoyuan loess-paleosol sequence of the western Chinese Loess Plateau over the last glacial-interglacial cycle and its geological implications. *Geochemistry, Geophysics, Geosystems*, *9*, Q04034. https://doi.org/10.1029/2007GC001928

Deng, C. L., Vidic, N. J., Verosub, K. L., Singer, M. J., Liu, Q. S., Shaw, J., & Zhu, R. X. (2005). Mineral magnetic variation of the Jiaodao Chinese loess/paleosol sequence and its bearing on long-term climatic variability. *Journal of Geophysical Research*, *110*, B03103. https://doi.org/10.1029/2004JB003451

Dunin-Borkowski, R. E., McCartney, M. R., Frankel, R. B., Bazylinski, D. A., Pósfai, M., & Buseck, P. R. (1998). Magnetic microstructure of magnetotactic bacteria by electron holography. *Science*, *282*(5395), 1868–1870. https://doi.org/10.1126/science.282.5395.1868

Dunlop, D. J. (2002). Theory and application of the Day plot (M_{rs}/M_s versus H_{cr}/H_c) 1. Theoretical curves and tests using titanomagnetite data. *Journal of Geophysical Research*, *107*(B3), 2056. https://doi.org/10.1029/2001JB000486

Egli, R. (2006). Theoretical aspects of dipolar interactions and their appearance in first-order reversal curves of thermally activated single-domain particles. *Journal of Geophysical Research*, *111*, B12S17. https://doi.org/10.1029/2006JB004567

Egli, R., Chen, A. P., Winklhofer, M., Kodama, K. P., & Horng, C.-S. (2010). Detection of noninteracting single domain particles using first-order reversal curve diagrams. *Geochemistry, Geophysics, Geosystems*, *11*, Q01Z11. https://doi.org/10.1029/2009GC002916

Egli, R., & Winklhofer, M. (2014). Recent developments on processing and interpretation aspects of first-order reversal curves (FORC). *Scientific Proceedings of Kazan Federal University*, *156*(1), 14–53.

Evans, M. E., & Heller, F. (2003). *Environmental Magnetism*. New York: Elsevier.

Fabian, K. (2003). Some additional parameters to estimate domain state from isothermal magnetization measurements. *Earth and Planetary Science Letters*, *213*(3-4), 337–345. https://doi.org/10.1016/S0012-821X(03)00329-7

Ferrat, M., Weiss, D. J., Strekopytov, S., Dong, S. F., Chen, H. Y., Najorka, J., et al. (2011). Improved provenance tracing of Asian dust sources using rare earth elements and selected trace elements for palaeomonsoon studies on the eastern Tibetan Plateau. *Geochimica Et Cosmochimica Acta*, *75*(21), 6374–6399.

Frankel, R. B., & Bazylinski, D. A. (2005). Magnetosomes: Nanoscale magnetic iron minerals in bacteria. In C. M. Niemeyer, & C. A. Mirkin (Eds.), *Nanobiotechnology: Concepts, Applications and Perspectives* (Vol. 10, pp. 136–145). Weinheim: Wiley-VCH Verlag GmbH & Co. KGaA. https://doi.org/10.1002/3527602453.ch10

Goiriena-Goikoetxea, M., García-Arribas, A., Rouco, M., Svalov, A. V., & Barandiaran, J. M. (2016). High-yield fabrication of 60 nm Permalloy nanodiscs in well-defined magnetic vortex state for biomedical applications. *Nanotechnology*, *27*(17), 175302. https://doi.org/10.1088/0957-4484/27/17/175302

Harrison, R. J., Dunin-Borkowski, R. E., & Putnis, A. (2002). Direct imaging of nanoscale magnetic interactions in minerals. *Proceedings of the National Academy of Sciences USA*, *99*(26), 16,556–16,561. https://doi.org/10.1073/pnas.262514499

Harrison, R. J., & Lascu, I. (2014). FORCulator: A micromagnetic tool for simulating first-order reversal curve diagrams. *Geochemistry, Geophysics, Geosystems*, *15*, 4671–4691. https://doi.org/10.1002/2014GC005582

Heslop, D., & Roberts, A. P. (2012). Estimation of significance levels and confidence intervals for first-order reversal curve distributions. *Geochemistry, Geophysics, Geosystems*, *13*, Q12Z40. https://doi.org/10.1029/2012GC004115

Heslop, D., Roberts, A. P., & Chang, L. (2014). Characterizing magnetofossils from first-order reversal curve (FORC) central ridge signatures. *Geochemistry, Geophysics, Geosystems*, *15*, 2170–2179. https://doi.org/10.1002/2014GC005291

Heslop, D., Roberts, A. P., Chang, L., Davies, M., Abrajevitch, A., & De Deckker, P. (2013). Quantifying magnetite magnetofossil contributions to sedimentary magnetizations. *Earth and Planetary Science Letters*, *382*, 58–65. https://doi.org/10.1016/j.epsl.2013.09.011

Hu, P. X., Liu, Q. S., Heslop, D., Roberts, A. P., & Jin, C. S. (2015). Soil moisture balance and magnetic enhancement in loess–paleosol sequences from the Tibetan Plateau and Chinese Loess Plateau. *Earth and Planetary Science Letters*, *409*, 120–132. https://doi.org/10.1016/j.epsl.2014.10.035

Isbell, R. F. (2002). *The Australian Soil Classification*. Collingwood, Victoria: CSIRO.

Jiang, Z. X., Liu, Q. S., Barrón, V., Torrent, J., & Yu, Y. J. (2012). Magnetic discrimination between Al-substituted hematites synthesized by hydrothermal and thermal dehydration methods and its geological significance. *Journal of Geophysical Research*, *117*, B02102. https://doi.org/10.1029/2011JB008605

Larrasoaña, J. C., Roberts, A. P., Chang, L., Schellenberg, S. A., Fitz Gerald, J. D., Norris, R. D., & Zachos, J. C. (2012). Magnetotactic bacterial response to Antarctic dust supply during the Paleocene–Eocene thermal maximum. *Earth and Planetary Science Letters*, *333-334*, 122–133. https://doi.org/10.1016/j.epsl.2012.04.003

Lascu, I., Harrison, R. J., Li, Y., Muraszko, J. R., Channell, J. E. T., Piotrowski, A. M., & Hodell, D. A. (2015). Magnetic unmixing of first-order reversal curve diagrams using principal component analysis. *Geochemistry, Geophysics, Geosystems*, *16*, 2900–2915. https://doi.org/10.1002/2015GC005909

Liu, Q. S., Deng, C. L., Torrent, J., & Zhu, R. X. (2007). Review of recent developments in mineral magnetism of the Chinese loess. *Quaternary Science Reviews*, *26*, 368–385. https://doi.org/10.1016/j.quascirev.2006.08.004

Maher, B. A. (2016). Palaeoclimatic records of the loess/paleosol sequences of the Chinese Loess Plateau. *Quaternary Science Reviews*, *154*, 23–84. https://doi.org/10.1016/j.quascirev.2016.08.004

Mayergoyz, I. D. (1991). *Mathematical Models of Hysteresis*. New York: Springer-Verlag.

Muxworthy, A., Heslop, D., & Williams, W. (2004). Influence of magnetostatic interactions on first-order-reversal-curve (FORC) diagrams: A micromagnetic approach. *Geophysical Journal International*, *158*, 888–897. https://doi.org/10.1111/j.1365-246X.2004.02358.x

Muxworthy, A., & Williams, W. (2005). Magnetostatic interaction fields in first-order-reversal-curve diagrams. *Journal of Applied Physics*, *97*, 063905. https://doi.org/10.1063/1.1861518

Muxworthy, A. R., & Dunlop, D. J. (2002). First-order reversal curve (FORC) diagrams for pseudo-single-domain magnetites at high temperature. *Earth and Planetary Science Letters*, *203*(1), 369–382. https://doi.org/10.1016/S0012-821X(02)00880-4

Muxworthy, A. R., King, J. G., & Heslop, D. (2005). Assessing the ability of first-order reversal curve (FORC) diagrams to unravel complex magnetic signals. *Journal of Geophysical Research*, *110*, B01105. https://doi.org/10.1029/2004JB003195

Muxworthy, A. R., & Williams, W. (2009). Critical superparamagnetic/single-domain grain sizes in interacting magnetite particles: Implications for magnetosome crystals. *Journal of the Royal Society Interface*, *6*, 1207–1212. https://doi.org/10.1098/rsif.2008.0462

Newell, A. J. (2005). A high-precision model of first-order reversal curve (FORC) functions for single-domain ferromagnets with uniaxial anisotropy. *Geochemistry, Geophysics, Geosystems*, *6*, Q05010. https://doi.org/10.1029/2004GC000877

Novosad, V., Guslienko, Y. K., Shima, H., Otani, Y., Fukamichi, K., et al. (2001). Nucleation and annihilation of magnetic vortices in sub-micron permalloy dots. *IEEE Transactions on Magnetics*, *37*(4), 2088–2090. https://doi.org/10.1109/20.951062

Pike, C., & Fernandez, A. (1999). An investigation of magnetic reversal in submicron-scale Co dots using first order reversal curve diagrams. *Journal of Applied Physics*, *85*(9), 6668–6676. https://doi.org/10.1063/1.370177

Pike, C. R., Roberts, A. P., Dekkers, M. J., & Verosub, K. L. (2001). An investigation of multi-domain hysteresis mechanisms using FORC diagrams. *Physics of the Earth and Planetary Interiors*, *126*(1-2), 11–25. https://doi.org/10.1016/S0031-9201(01)00241-2

Pike, C. R., Roberts, A. P., & Verosub, K. L. (1999). Characterizing interactions in fine magnetic particle systems using first order reversal curves. *Journal of Applied Physics*, *85*(9), 6660–6667. https://doi.org/10.1063/1.370176

Pike, C. R., Roberts, A. P., & Verosub, K. L. (2001). First-order reversal curve diagrams and thermal relaxation effects in magnetic particles. *Geophysical Journal International*, *145*(3), 721–730. https://doi.org/10.1046/j.0956-540x.2001.01419.x

Plaza-Morlote, M., Rey, D., Santos, J. F., Ribeiro, S., Heslop, D., Bernabeu, A., et al. (2017). Southernmost evidence of large European Ice Sheet-derived freshwater discharges during the Heinrich Stadials of the Last Glacial Period (Galician Interior Basin, Northwest Iberian Continental Margin). *Earth and Planetary Science Letters*, *457*, 213–226. https://doi.org/10.1016/j.epsl.2016.10.020

Porter, S. C., & An, Z. S. (1995). Correlation between climate events in the North-Atlantic and China during Last Glaciation. *Nature*, *375*(6529), 305–308. https://doi.org/10.1038/375305a0

Rangin, C., Silver, E., & von Breymann, M. T. (1990). Site 769). *Proceedings of the Ocean Drilling Program, Initial Reports* (Vol. 124). College Station, TX: Ocean Drilling Program.

Raymond, O. L., Liu, S., Gallagher, R., Highet, L. M., & Zhang, W. (2012). *Surface Geology of Australia* (scale 1:1000000, 2012 ed.). Commonwealth of Australia, Canberra: Geoscience Australia.

Roberts, A. P. (2015). Magnetic mineral diagenesis. *Earth-Science Reviews*, *151*, 1–47. https://doi.org/10.1016/j.earscirev.2015.09.010

Roberts, A. P., Almeida, T. P., Church, N. S., Harrison, R. J., Heslop, D., Li, Y. L., et al. (2017). Resolving the origin of pseudo-single domain magnetic behavior. *Journal of Geophysical Research: Solid Earth*, *122*, 9534–9558. https://doi.org/10.1002/2017JB014860

Roberts, A. P., Chang, L., Heslop, D., Florindo, F., & Larrasoaña, J. C. (2012). Searching for single domain magnetite in the "pseudo-single-domain" sedimentary haystack: Implications of biogenic magnetite preservation for sediment magnetism and relative paleointensity determinations. *Journal of Geophysical Research*, *117*, B08104. https://doi.org/10.1029/2012JB009412

Roberts, A. P., Florindo, F., Chang, L., Heslop, D., Jovane, L., & Larrasoaña, J. C. (2013). Magnetic properties of pelagic marine carbonates. *Earth-Science Reviews*, *127*, 111–139. https://doi.org/10.1016/j.earscirev.2013.09.009

Roberts, A. P., Florindo, F., Villa, G., Chang, L., Jovane, L., Bohaty, S. M., et al. (2011). Magnetotactic bacterial abundance in pelagic marine environments is limited by organic carbon flux and availability of dissolved iron. *Earth and Planetary Science Letters*, *310*, 441–452. https://doi.org/10.1016/j.epsl.2011.08.011

Roberts, A. P., Heslop, D., Zhao, X., & Pike, C. R. (2014). Understanding fine magnetic particle systems through use of first-order reversal curve diagrams. *Reviews of Geophysics*, *52*, 557–602. https://doi.org/10.1002/2014RG000462

Roberts, A. P., Liu, Q. S., Rowan, C. J., Chang, L., Carvallo, C., Torrent, J., & Horng, C.-S. (2006). Characterization of hematite (α-Fe_2O_3), goethite (α-FeOOH), greigite (Fe_3S_4), and pyrrhotite (Fe_7S_8) using first-order reversal curve diagrams. *Journal of Geophysical Research*, *111*, B12S35. https://doi.org/10.1029/2006JB004715

Roberts, A. P., Pike, C. R., & Verosub, K. L. (2000). First-order reversal curve diagrams: A new tool for characterizing the magnetic properties of natural samples. *Journal of Geophysical Research*, *105*(B12), 28,461–28,475. https://doi.org/10.1029/2000JB900326

Schabes, M. E., & Bertram, H. N. (1988). Magnetization processes in ferromagnetic cubes. *Journal of Applied Physics*, *64*(3), 1347–1357. https://doi.org/10.1063/1.341858

Viscarra Rossel, R. A., Bui, E. N., de Caritat, P., & McKenzie, N. J. (2010). Mapping iron oxides and the color of Australian soil using visible–near-infrared reflectance spectra. *Journal of Geophysical Research*, *115*, F04031. https://doi.org/10.1029/2009JF001645

Yu, Y. J., & Tauxe, L. (2005). On the use of magnetic transient hysteresis in paleomagnetism for granulometry. *Geochemistry, Geophysics, Geosystems*, *6*, Q01H14. https://doi.org/10.1029/2004GC000839

Zhao, X., Heslop, D., & Roberts, A. P. (2015). A protocol for variable-resolution first-order reversal curve measurements. *Geochemistry, Geophysics, Geosystems*, *16*, 1364–1377. https://doi.org/10.1002/2014GC005680

Zhao, X., Roberts, A. P., Heslop, D., Paterson, G. A., Li, Y. L., & Li, J. H. (2017). Magnetic domain state diagnosis using hysteresis reversal curves. *Journal of Geophysical Research: Solid Earth*, *122*, 4767–4789. https://doi.org/10.1002/2016JB013683